A COMPUTATIONAL STUDY OF RECONSTRUCTION ALGORITHMS FOR SYNTHETIC APERTURE DIFFRACTION TOMOGRAPHY : INTERPOLATION VERSUS INTERPOLATION-FREE

Jian-Yu Lu

Department of Biomedical Engineering
Nanjing Institute of Technology
Nanjing, China

INTRODUCTION

X-ray computerized tomograpy (X-CT) has been a great success in medical diagnoses [1-7]. Its finders, Hounsfield (English) and Cormack (American), had got Nobel Prize In physiology and medicine in 1979. But, X-CT is harmful to human body because large dosage of the X-ray is used. In addition, the equipment of X-CT is very expensive. In order to overcome the disadvantages of X-CT, people developed the ultrasonic computerized tomography (U-CT) [8]. Compared to X-ray, the wavelength of the ultrasound is much longer and, thus, the diffraction effects of the ultrasound are remarkable. In order to solve the diffraction problem of the ultrasound in U-CT, people developed the concept of ultrasonic diffraction computerized tomography (DUCT) [9-10], and, after then, many reconstruction algorithms for DUCT have been developed and further studied [11-18].

The concept of DUCT is directly based on the inversion of wave equation under the weak scattering assumption (i.e. the scattered wave is much smaller than the incident wave). Conventional ultrasonic diffraction computerized tomography uses the method analogous to that used in commercial X-CT. A plane-wave is insonified on an object to be imaged and is rotated 360° around the object. For each position of the rotation, a diffraction projection will be obtained (usually, we call such a projection a view). Thus, as the incident wave rotates, many projections will be obtained. From these projections, the images can be reconstructed. The advantage of the conventional DUCT is that high quality images can be obtained by relatively less projections and less points contained in each projection. This is because relatively more information of the spectrum of the object can be obtained by using this measuring geometry. But, the conventional DUCT requires its measuring system rotating 360° around the object, and is not applicable when obstacles exist in the path of the rotation. In addition, it requires a large scale plane-wave insonification, which will be difficult if it is used in practical medical imaging.

In order to overcome the disadvantages of the conventional DUCT, D.Nahamoo et al. [16] put forward a new type of DUCT — the synthetic aperture diffraction computerized tomography (SADCT). In SADCT, for a good image reconstruction, the measuring system is only needed to rotate around the object once and, in principle, any kind of insonifications can be used. Furthermore, in reference [15], D.Nahamoo et al. developed an interpolation-free reconstruction algorithm (IFRA) for SADCT and performed its computer simulation study. But, because this algorithm containes a space-variant filter, it requires large amount of computations. For an NxN image reconstructed by NxN diffracted data, this algorithm requires approximatly $O(N^3+N^2\log_2 N)$ complex multiplications. Besides, even if for a rather big value of N, such as, N=128, the reconstructed image is still not satisfied. In order to reduce the number of the complex mutiplications and to improve the image reconstructions, we used Fourier-domain interpolation reconstruction algorithms (FDIRAs) for the reconstruction of SADCT, and performed a detailed computational study of these algorithms. For an NxN image reconstructed by NxN diffracted data, the FDIRAs require only approximately $O(N^2\log_2 N)$ complex multiplications, and, the larger the N is, the more the computation is saved. From the results of the computational study of SADCT, one can see that the quality of the images reconstructed by FDIRAs is better than that reconstructed by IFRA. In addition, in FDIRAs, the nearest-neighbor interpolation reconstruction algorithm, in general, will give better results than the bilinear interpolation reconstruction algorithm. But, this is not the case for the conventional DUCT, where the Fourier-doamin bilinear interpolation reconstruction algorithm gives better results than the nearest-neighbor interpolation reconstruction algorithm. This conclusion was demonstrated in reference [11] and has been re-proved by us in this paper.

In the computational study of FDIRAs, we discovered that better reconstructions would be obtained when the shift of the coordinate of the object was performed before the Fourier-domain interpolations, and, we also discovered that the accuracy of the interpolations of the points near the boundaries of the Fourier-domain coverage areas A or B (see Fig.2) had a great influence on the reconstructions.

In this paper, all the reconstructed images will be quantitatively evaluated by distance criteria as well as reconstructed values on a line through three smallest ellipses of the phantom used in our computer simulation.

This paper is organized as follows : First, we will state simply the basic principles of SADCT and obtain two diffraction projection formulas. Next, we will introduce FDIRAs and derive the relationships between curvilinear and rectangular coordinates. Then, we will give the results of the computer simulation and the comparisons among these results. Finally, we will make a brief summary of this paper.

BASIC PRINCIPLES FOR SADCT

Wave Equation

In this paper, we consider only the two-dimensional case,

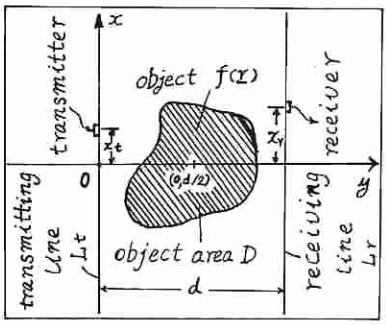

Fig.1 *The datum acqusition geometry of the SADCT*

i.e., we assume that the object is not varied with the axis z (the axis z is normal to the x-y plane shown in Fig.1). The coordinates x_t and x_r in Fig.1 represent the positions of the transmitter and the receiver on the transmitting line L_t and the receiving line L_r, respectively, and the center of the object is sited at the point (0,d/2). The transmitter can be moved to N positions on the transmitting line L_t, and for each transmitter position, the receiver can also be moved to N positions on the receiving line L_r. Thus, by using this datum acquisition system, NxN diffracted data will be obtained.

We now confine our discussion to soft bio-tissues. We assume that the object is immersed in the surrounding homogeneous medium (such as water), and the ultrasonic field in the area between the two lines L_t and L_r is governed approximatly by the inhomogeneous Helmholtz equation

$$(\nabla^2+k_o^2)u(\underline{r})=-f(\underline{r})u(\underline{r}) \tag{1}$$

where ∇^2 is the Laplacian operator; $u(\underline{r})$ represents the total complex wave field at the point $\underline{r}=(x,y)$; k_o is the wave number of the surrounding homogeneous medium; and $f(\underline{r})$ is the object function. $f(\underline{r})$ is related to the distribution of a refrative index $n(\underline{r})$ by

$$f(\underline{r})=\begin{cases} k_o^2[n^2(\underline{r})-1] & , \ \underline{r}\in D \\ 0 & , \text{ otherwise} \end{cases} \tag{2}$$

and $f(\underline{r})$ will be a real function if the attenuation of the object is not considered. (In the following, we will not consider the attenuation of the object).

Solution of Helmholtz Equation and Born Approximation

The total wave field $u(\underline{r})$ in Eq.(1) can be written as the sum of the incident field $u_i(\underline{r})$ and the scattered field $u_s(\underline{r})$ [16]

$$u(\underline{r})=u_i(\underline{r})+u_s(\underline{r}) \tag{3}$$

where $u_s(\underline{r})$ is given by [15]

$$u_s(\underline{r})=\int_D f(\underline{r}_o)u(\underline{r}_o)G(\underline{r}|\underline{r}_o)d\underline{r}_o \tag{4}$$

and D is the area shown in Fig.1; $G(\underline{r}|\underline{r}_o)$ is the Green function associated with the datum acquisition system. Here, we assume $G(\underline{r}|\underline{r}_o)$ is a two-dimensional free-space Green function, and can be expressed as [20]

$$G(\underline{r}|\underline{r}_o)= \frac{j}{4} H_o(k_o|\underline{r}-\underline{r}_o|) \tag{5}$$

where H_o is the zero order Hankel function with the first kind; and $|\underline{r}-\underline{r}_o|$ is the distance between the field point $\underline{r}=(x,y)$ and the source point $\underline{r}_o=(x_o,y_o)$.

We further assume that the Born approximation is held, i.e., the weak scattering assumption is satisfied

$$|u_s(\underline{r})| << |u_i(\underline{r})| \tag{6}$$

Under the condition of the Born approximation, the total field $u(\underline{r})$ in Eq.(4) may be simply replaced by the incident field $u_i(\underline{r})$

$$u_s(\underline{r})= \frac{j}{4} \int_D f(\underline{r}_o)u_i(\underline{r}_o)H_o(|\underline{r}-\underline{r}_o|)d\underline{r}_o \tag{7}$$

Thus, from Eq.(7), we obtain the weak scattering solution of the Helmholtz equation (1).

Diffraction Projection Formulas for SADCT

Let $u_i(\underline{r};x_t)$ represent the incident field at the point $\underline{r}$ with the transmitter located at the point $(x_t,0)$, by using the angular spectrum expansion [19,21], and through simple derivations [15], one obtains

$$u_i(\underline{r};x_t)= \frac{1}{2\pi} \int_{-\infty}^{\infty} A_t(k_x)e^{-jk_x x_t} e^{j\underline{K}\cdot\underline{r}} dk_x \tag{8}$$

where $A_t(k_x)$ is the Fourier transform of the function $u_i(x,0;0)$ which is the incident field on the transmitting line L_t while the transmitter is placed at the origin of the coordinate shown in Fig.1

$$A_t(k_x)= \int_{-\infty}^{\infty} u_i(x,0;0)e^{-jk_x x} dx \tag{9}$$

where $\underline{K}=(k_x,k_y)$, and

$$k_y=\sqrt{k_o^2-k_x^2} \tag{10}$$

H_o in Eq.(7) can also be expanded by the angular spectrum expansion [21]

$$H_o(k_o|\underline{r}-\underline{r}_o|)= \frac{1}{\pi} \int_{-\infty}^{\infty} \frac{e^{j\underline{T}\cdot(\underline{r}-\underline{r}_o)}}{t_y} dt_x \tag{11}$$

where $\underline{T}=(t_x,t_y)$, and

$$t_y=\sqrt{k_o^2-t_x^2} \tag{12}$$

Substituting Eqs.(8) and (11) into Eq.(7), and using the notation $u_s(x_r;x_t)$ to represent the received scattered field at the point $\underline{r}=(x_r,d)$, one obtains

$$u_s(x_r;x_t)=\frac{1}{(2\pi)^2}\iint_{-\infty}^{\infty}\frac{je^{jt_yd}}{2t_y}A_t(k_x)\Big[\int_D f(\underline{r}_o)e^{-j(\underline{T}-\underline{K})\cdot\underline{r}_o}d\underline{r}_o\Big]e^{j(t_xx_r-k_xx_t)}dt_xdk_x \tag{13}$$

Let $U_s(t_x;k_x)$ be the Fourier transform of $u_s(x_r;-x_t)$, one obtains

$$U_s(t_x;k_x)=\frac{je^{jt_yd}}{2t_y}A_t(k_x)\int_D f(\underline{r}_o)e^{-j(\underline{T}-\underline{K})\cdot\underline{r}_o}d\underline{r}_o \tag{14}$$

If we take the filtering properties of the receiver into account and define $P_{sa}(t_x;k_x)$ as the Fourier transform of the scattered field received, we have

$$P_{sa}(t_x;k_x)=\frac{je^{jt_yd}}{2t_y}A_r(t_x)A_t(k_x)\int_D f(\underline{r}_o)e^{-j(\underline{T}-\underline{K})\cdot\underline{r}_o}d\underline{r}_o \tag{15}$$

where $A_r(t_x)$ is the filter function of the receiver. The integral on the right hand side of Eq.(15) represent the Fourier transform of $f(\underline{r})$ evaluated on the curvilinear coordinate : $\{\underline{T}-\underline{K};\ |t_x|\leq k_o, |k_x|\leq k_o\}$, and is defined as $F(\underline{T}-\underline{K})$. From Eq.(15), we obtain the diffraction projection formula

$$F(\underline{T}-\underline{K})=-\frac{2jt_ye^{-jt_yd}}{A_r(t_x)A_t(k_x)}P_{sa}(t_x;k_x) \tag{16}$$

In order to make the Fourier space covered sufficiently by the data measured, we must rotate the measuring system or the objet 90° around the point (0,d/2) once. According to the similar derivations given above, and defining the notation $P_{sb}(t_x;k_x)$ as the Fourier transform of the scattered field measured after the 90° rotation, we obtain another diffraction projection formula

$$F[Q^{-1}(\underline{T}-\underline{K})]=-\frac{2jt_ye^{-jt_yd}}{A_r(t_x)A_t(k_x)}P_{sb}(t_x;k_x) \tag{17}$$

where Q is a 90° rotation matrix, and Q^{-1} is its inversion

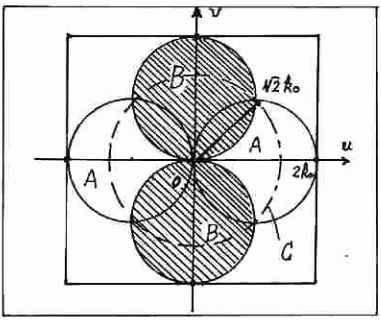

Fig.2 The Fourier-domain coverages. The area A and B (hatched) are the coverage before and after the 90° rotation of the measuring system, respectively

$$Q = \begin{bmatrix} 0 & , & -1 \\ 1 & , & 0 \end{bmatrix} \tag{18}$$

From Eqs.(16) and (17) and by using the inverse Fourier transform, the object function $f(\underline{r})$ can be reconstructed.

FOURIER-DOMAIN INTERPOLATION RECONSTRUCTION ALGORITHMS

Fourier-Domain Coverages

Suppose that u-v is a rectangular coordinate on the Fourier space and $\underline{W}=\underline{T}-\underline{K}$, where $\underline{W}=(u,v)$ represents a vector at the point (u,v), and according to Eqs.(10) and (12), one obtains

$$\begin{cases} u=t_x-k_x \\ v=t_y-k_y \end{cases} \tag{19}$$

After the 90° rotation of the measuring system, if we define $\underline{W}=Q^{-1}(\underline{T}-\underline{K})$, from Eqs.(10), (12) and (18), we obtain

$$\begin{cases} u= t_y-k_y \\ v=-t_x+k_x \end{cases} \tag{20}$$

where $|t_x|\leqslant k_o$ and $|k_x|\leqslant k_o$. For the case $|t_x|>k_o$ or $|k_x|>k_o$, the scattered wave is not a propagation wave, but really an attenuated field. If the receiving line L_r is placed several wavelengths, say, ten wavelengths away from the object, the effects of the attenuated field is negligible. By the way, we will state that the Eqs.(16) and (17) are held only when the conditions $|t_x|\leqslant k_o$ and $|k_x|\leqslant k_o$ are satisfied.

The Fourier-domain coverage areas A and B can be obtained from Eqs.(19) and (20), respectively, as shown in Fig.2

Relationships Between Curvilinear and Rectangular Coordinates

In order to perform the Fourier-domain interpolations, we

must find the relationships between the curvilinear and the rectangular coordinates. From Eqs.(12) and (10), we know that $t_y \geq 0$ and $k_y \geq 0$, and we obtain

$$t_x^2 + t_y^2 = k_o^2 \tag{21}$$

$$k_x^2 + k_y^2 = k_o^2 \tag{22}$$

From Eq.(19), we obtain

$$\begin{cases} (u-t_x)^2 + (v-t_y)^2 = k_o^2 & (23) \\ (u+k_x)^2 + (v+k_y)^2 = k_o^2 & (24) \end{cases}$$

Eq.(23) represents the circles centered at (t_x, t_y), with radius of k_o, on the u-v plane. The trace of the center of these circles (t_x, t_y) is also a circle but centered at origin, with radius k_o, on the u-v plane, defined by Eq.(21). Because $t_y \geq 0$, Eq.(21) represents only the super-half of the circle. Similarly, Eq.(24) represents the circles centered at $(-k_x, -k_y)$, with radius of k_o, on the u-v plane. The trace of the center of these circles $(-k_x, -k_y)$ is on the lower-half of the circle defined by Eq.(22). All the points (u,v) which satisfy Eqs.(23) and (24) simultaneously will form a set which will cover the area A shown in Fig.2. From Eqs.(21) to (24), we will obtain the relationships between a point (t_x, k_x) on the curvilinear coordinate and a point (u,v) on the rectangular coordinate (See Fig.3).

If a point (u,v) belongs to the first or the third quarter of the coordinate u-v, one obtains

$$\begin{cases} t_x = \frac{1}{2}(u-q1) \\ k_x = -\frac{1}{2}(u+q1) \end{cases} \tag{25}$$

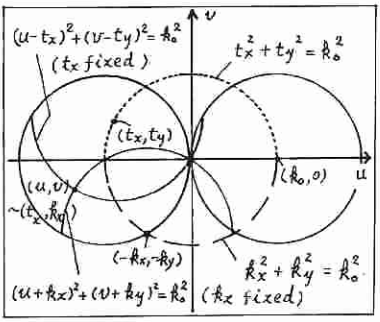

Fig.3 The relationships between the curvilinear and the rectangular coordinates

where

$$q1 = |v| \cdot \sqrt{\frac{4k_o^2}{u^2+v^2} - 1} \tag{26}$$

If a point (u,v) belongs to the second or the fourth quarter of the coordinate u-v, one obtains

$$\begin{cases} t_x = \dfrac{1}{2}(u+q1) \\ k_x = -\dfrac{1}{2}(u-q1) \end{cases} \tag{27}$$

From Eq.(20), one obtains

$$\begin{cases} (u-t_y)^2 + (v+t_x)^2 = k_o^2 & (28) \\ (u+k_y)^2 + (v-k_x)^2 = k_o^2 & (29) \end{cases}$$

Similarly, we will obtain the relationships between a point (t_x,k_x) on the curvilinear coordinate and a point (u,v) on the rectangular coordinate in area B (the area B is formed by a set of the points (u,v)s which satisfy the Eqs.28 and 29 simultaneously as shown in Fig.2). If a point (u,v) belongs to the first or the third quarter of the coordinate u-v, one obtains

$$\begin{cases} t_x = -\dfrac{1}{2}(v-q2) \\ k_x = \dfrac{1}{2}(v+q2) \end{cases} \tag{30}$$

where

$$q2 = |u| \cdot \sqrt{\frac{4k_o^2}{u^2+v^2} - 1} \tag{31}$$

If a point (u,v) belongs to the second or the fourth quarter of the coordinate u-v, one obtains

$$\begin{cases} t_x = -\dfrac{1}{2}(v+q2) \\ k_x = \dfrac{1}{2}(v-q2) \end{cases} \tag{32}$$

Bilinear Interpolation and Nearest-Neighbor Interpolation

In order to reconstruct the object function $f(\underline{r})$ from its Fourier transform $F(\underline{W})$ using IFFT, we must know the values of $F(\underline{W})$ on rectanglar grids. To arrive this, we use two com-

monly used interpolation methods : the bilinear interpolation and the nearest-neighbor interpolation. The bilinear interpolation formula is given by

$$P_S(t_x;k_x)=\sum_{i=1}^{N_{t_x}}\sum_{j=1}^{N_{k_x}}P_S(t_{x_i};k_{x_j})h1(t_x-t_{x_i})h2(k_x-k_{x_j}) \quad (33)$$

where $(t_{x_i};k_{x_j})$ are the discrete points on the t_x-k_x plane, on which the values of the function $P_S(\underline{T}-\underline{K})$ are known. N_{t_x} and N_{k_x} are the numbers of the discrete points of t_x and k_x respectively, and h1 and h2 are given by (here, $\Delta t_x=\Delta k_x=$const.)

$$h1(t_x-t_{x_i})=\begin{cases}1-\dfrac{|t_x-t_{x_i}|}{\Delta t_x}, & |t_x-t_{x_i}|\leq\Delta t_x=t_{x_{i+1}}-t_{x_i}\\ 0, & \text{otherwise}\end{cases}$$

$$h2(k_x-k_{x_j})=\begin{cases}1-\dfrac{|k_x-k_{x_j}|}{\Delta k_x}, & |k_x-k_{x_j}|\leq\Delta k_x=k_{x_{j+1}}-k_{x_j}\\ 0, & \text{otherwise}\end{cases} \quad (34)$$

The procedures of the bilinear interpolation are given below. Given a grid point (u,v) on the rectangular coordinate, if it belongs to the area A, we will calculate the corresponding point (t_x,k_x) on the curvilinear coordinate according to Eqs.(25) or (27), and then calculate $P_{SA}(t_x;k_x)$ using Eq.(33), finally, we will find the Fourier transform of the object function $F(\underline{W})$ from the Eq.(16); If the point (u,v) belongs to the area B, we will calculate (t_x,k_x) according to Eqs.(30) and (32), and then, using Eqs.(33) and (17), we will obtain the value of $F(\underline{W})$ at the point (u,v); If the point (u,v) belongs to $A\cap B$, we will average these two interpolation resultes and assign it to $F(\underline{W})$ at this point. (The interpolations of points near the boundaries of the areas A or B (see Fig.2) will be specially considered in next section.)

The procedures of the nearest-neighbor interpolation are the same as those of the bilinear interpolation except that after the point (t_x,k_x) is calculated, the value of the Fourier transform of the object function on the point $(t_{x_{i_0}},k_{x_{j_0}})$ (which is the nearest-neighbor of the point (t_x,k_x) among the points (t_{x_i},k_{x_j}) $(i=1,2,\ldots,N_{t_x},\ j=1,2,\ldots,N_{k_x})$ on which the Fourier transform of the object function are known) is taken as the value of the Fourier transform of the object function on the point (t_x,k_x).

In order to diminish the Gibbs oscillation, we apply a two-dimensional blackman window $b(\underline{W})$ to the function $F(\underline{W})$ prior to IFFT

$$b(\underline{W})=\begin{cases}0.42-0.5\cos\dfrac{2\pi r}{2\sqrt{2}k_o}+0.08\cos\dfrac{4\pi r}{2\sqrt{2}k_o}, & |\underline{W}|\leq\sqrt{2}k_o\\ 0, & |\underline{W}|>\sqrt{2}k_o\end{cases} \quad (35)$$

where

$$r=\sqrt{u^2+v^2}+\sqrt{2}k_o \quad (35')$$

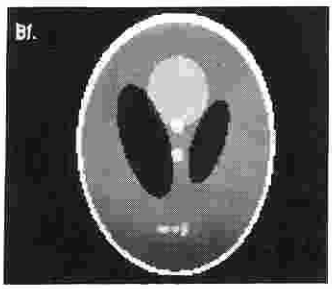

Fig.4 *The 128x128 head phantom image used in our computer simulation*

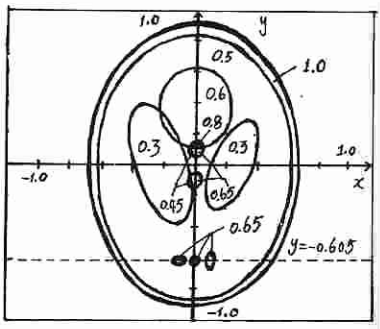

Fig.5 *The gray level asignment of the phantom. The dashed line through the phantom is the line y=-0.605*

If we take the 2-D IFFT of the function $F(\underline{W})b(\underline{W})$, we will obtain the low-pass filtered version of the object function $f(\underline{r})$.

COMPUTER SIMULATION RESULTS OF THE FOURIER-DOMAIN INTERPOLATION AND INTERPOLATION-FREE RECONSTRUCTION ALGORITHMS

The Phantom Used in Our Computer Simulation

The phantom used in our computer simulation was the same as that used by Shepp and Logan [22], but had the gray level assignment changed to those used by Devaney [13] and Pan and Kak [11]. The image of the phantom and the gray level assignment of the phantom are shown in Figs.4 and 5, respectively.

Definition of the Distance Criteria

For the convenience of the quantitative comparision of the reconstructed images and the phantom, we have adopted the distance criteria defined in [7] and defined the average adjusted version of them. The definitions of these distance criteria are given by

$$d1=\sqrt{\frac{\sum_{i=1}^{128}\sum_{j=1}^{128}(r_{ij}-p_{ij})^2}{\sum_{i=1}^{128}\sum_{j=1}^{128}(p_{ij}-\overline{p})^2}} \tag{36}$$

$$r1=\frac{\sum_{i=1}^{128}\sum_{j=1}^{128}|r_{ij}-p_{ij}|}{\sum_{i=1}^{128}\sum_{j=1}^{128}|p_{ij}|} \tag{37}$$

$$e1=\max_{\substack{1<I<64\\1<J<64}}|r_{IJ}-p_{IJ}| \tag{38}$$

where

$$r_{IJ} = \frac{1}{4} (r_{2I,2J} + r_{2I+1,2J} + r_{2I,2J+1} + r_{2I+1,2J+1}) \qquad (39)$$

$$p_{IJ} = \frac{1}{4} (p_{2I,2J} + p_{2I+1,2J} + p_{2I,2J+1} + p_{2I+1,2J+1}) \qquad (40)$$

r_{ij} and p_{ij} in the above equations are pixel values of the reconstructed images and the phantom for the ith row and the jth column respectively, while $\bar{r}$ and $\bar{p}$ are the average values of the reconstructed images and the phantom respectively

$$\bar{r} = \frac{1}{128 \times 128} \sum_{i=1}^{128} \sum_{j=1}^{128} r_{ij} \qquad (41)$$

$$\bar{p} = \frac{1}{128 \times 128} \sum_{i=1}^{128} \sum_{j=1}^{128} p_{ij} \qquad (42)$$

If the reconstructed image is the phantom, the distance critera d1, r1 and e1 will be all equal to zero. Therefore, the smaller the distance critera are, the better the reconstructed images will be. The three distance criteria reflect the different nature of the errors of the reconstructed images. d1 is sensitive to the individual large errors of the reconstructed image; r1 is sensitive to the accumulation of the small errors; while e1 indicates the maximum error of the elements of the reconstructed images, which is important for the quantitative image reconstructions (for obtaining the distance criterion e1, we have chosen the average of every four pixel values as the value of one element of a reconstructed image, the element represents part of the tissues and is usually of the size of several pixels).

If the images reconstructed have their averages different from the average of the phantom, we will use the average adjusted version of the distance criteria defined above. The average adjusted version of the distance criteria are defined and calculated as follows. First, we calculate the averages $\bar{r}$ and $\bar{p}$ of the reconstructed image and the phantom according to Eqs.(41) and (42), respectively, and then we add the difference between $\bar{p}$ and $\bar{r}$ to every pixel of the reconstructed image, and finally, we re-calculate the distance critera using Eqs.(36), (37) and (38) and define the newly calculated average adjusted distance critera as d2, r2 and e2, respectively. From the definition of the average adjusted distance criteria, one may see that the average adjusted distances get rid of the factor of the shift of the averages of the reconstructed images and, therefore, they are more closely connected to the qualities of the reconstructed images shown on a monitor (because the brightness of the images shown on the monitor can be adjusted arbitrarily to make the images looked better). In this paper, we will using following eight criteria d1, r1, e1, d2, r2, e2, max and min for all the images reconstructed. The notations max and min represent the maximun and the minimun values of the reconstructed images before the

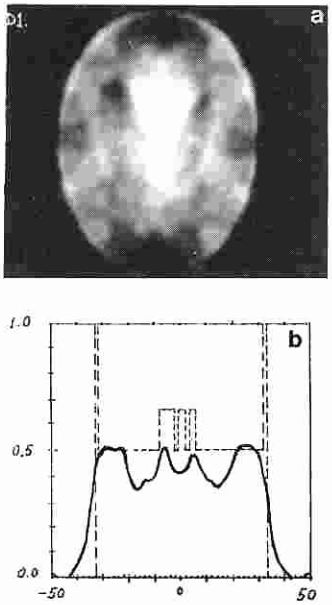

Fig.6 (a) The reconstructed 128x128 image with N=64 for the SADCT (Bilinear) (b) Numerical comparison on the line y=-0.605 (See Fig.5)

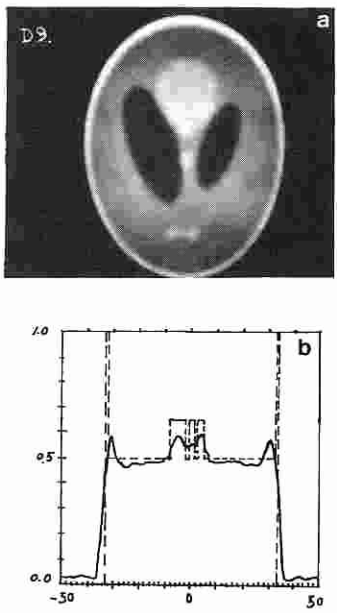

Fig.8 (a) The reconstructed 128x128 image with N=256 for the SADCT (Bilinear) (b) Numerical comparison on the line y=-0.605 (See Fig.5)

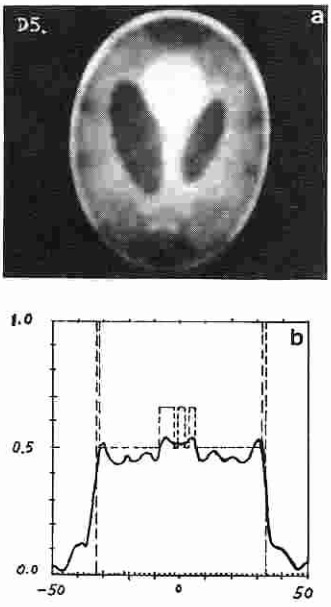

Fig.7 (a) The reconstructed 128x128 image with N=128 for the SADCT (Bilinear) (b) Numerical comparison on the line y=-0.605 (See Fig.5)

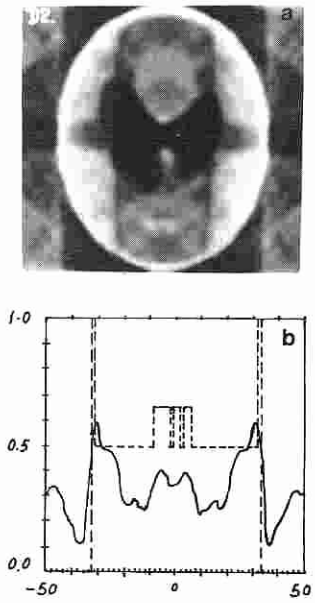

Fig.9 (a) The reconstructed 128x128 image with N=64 for the SADCT (Nearest-neighbor) (b) Numerical comparison on the line y=-0.605 (See Fig.5)

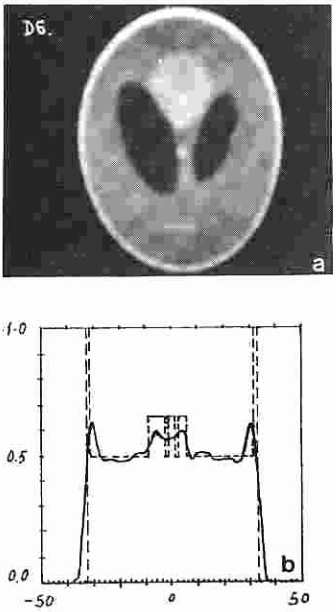

Fig.10 (a) The reconstructed 128x128 image with N=128 for the SADCT (Nearest-neighbor) (b) Numerical comparison on the line y=-0.605 (See Fig.5)

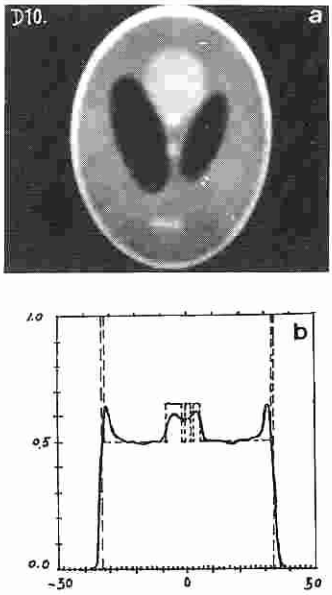

Fig.11 (a) The reconstructed 128x128 image with N=256 for the SADCT (Nearest-neighbor) (b) Numerical comparison on the line y=-0.605 (See Fig.5)

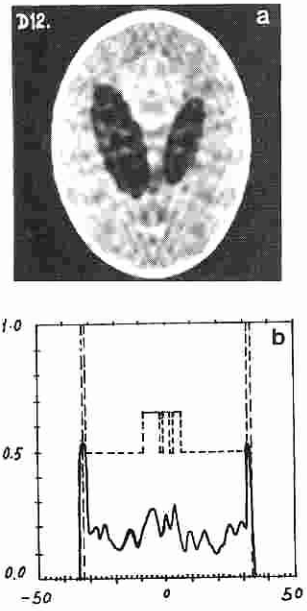

Fig.12 (a) The reconstructed 128x128 image with N=128 for the SADCT (Interpolation-free) (b) Numerical comparison on the line y=-0.605 (See Fig.5)

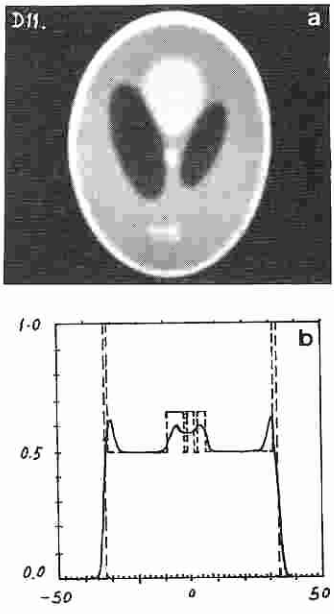

Fig.13 (a) The 128x128 image reconstructed from the windowed 128x128 Fourier-domain grids (delta=4k0/128) (b) numerical comparison on the line y=-0.605 (See Fig.5)

Table 1. The distances of the images reconstructed by the FDIRAs and the IFRA for the SADCT

Fig.	N	Interpolation	d1	r1	e1	d2	r2	e2	max	min
6	64	Bilinear	0.6355	0.4781	0.7959	0.6355	0.4781	0.7958	1.090	-0.2864
9	64	Nearest-Neighbor	0.9571	0.9100	0.6181	0.9570	0.9105	0.6139	0.8422	-0.2703
7	128	Bilinear	0.4659	0.3179	0.6089	0.4659	0.3179	0.6087	0.8364	-0.1203
10	128	Nearest-Neighbor	0.3367	0.1634	0.4617	0.3367	0.1634	0.4616	0.9202	-4.976×10^{-2}
8	256	Bilinear	0.3608	0.1943	0.5224	0.3608	0.1943	0.5223	0.8310	-4.943×10^{-2}
11	256	Nearest-Neighbor	0.3310	0.1421	0.4661	0.3310	0.1422	0.4659	0.9125	-2.593×10^{-2}
12	128	Interpolation-free	1.041	1.010	0.8365	0.5091	0.4224	0.6020	0.7724	-0.4149
13	/	Direct-calculation	0.3288	0.1228	0.4586	0.3288	0.1231	0.4584	0.9209	2.268×10^{-4}

adjustment of the averages of these images.

The Comparison of FDIRAs and IFRA

Figs.6(a), 7(a) and 8(a) show the 128x128 images reconstructed by the Fourier-domain bilinear interpolation reconstruction algorithm with N=64, 128 and 256, respectively; while Figs.9(a), 10(a) and 11(a) are the same as Figs.6(a), 7(a) and 8(a) respectively, except that they were reconstructed by the nearest-neighbor interpolation reconstruction algorithm. Fig.12(a) shows the 128x128 image reconstructed by IFRA, and Fig.13(a) is the 128x128 image reconstructed by direct calculation of the Fourier transform of the phantom on the rectangular grids. The sampling interval of Fig.13(a) on the Fourier-domain was taken as delta=$4k_o/128$. Fig.13(a) is the best image which can be obtained by DUCT with the use of 2-D blackman window of radius $\sqrt{2}k_o$ and this sampling interval. Figs.6(b) to 13(b) are the comparisons of the reconstructed values (real lines) and the real values (dashed lines) on the line y=-0.605 (see Fig.5) corresponding to Figs.6(a) to 13(a), respectively.

From Figs.7, 10 and 12, we can see that FDIRAs give better image reconstructions than IFRA with N=128 (for SADCT, the reconstructions will not be good if N is less than 128, this can be seen from Figs.6 and 9). From the comparison of Figs.8, 11, and Fig.9 in reference [15], the same conclusion will be obtained. In addition, we can see that the reconstructions obtained by the nearest-neighbor interpolation algorithm are better than those obtained by the bilinear interpolation, except for the case of N=64. These conclusions can also be seen clearly from table 1 (Table 1 shows the comparison of the distances of the reconstructed images from Figs.6 to 13). By the way, we shall state that the quality of the image of Fig.11 (N=256) is very close to its limit reconstruction

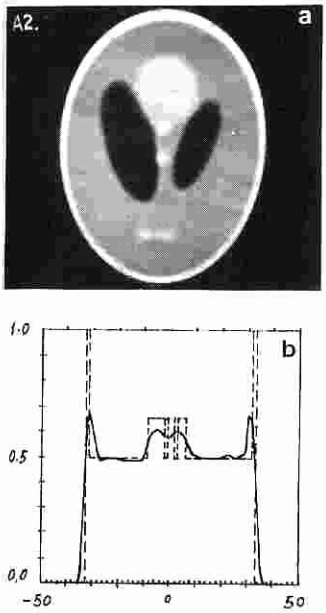

Fig.14 (a) The reconstructed 128x128 image with 360° rotated plane-wave insonification (Bilinear) (b) Numerical comparison on the line y=-0.605 (See Fig.5)

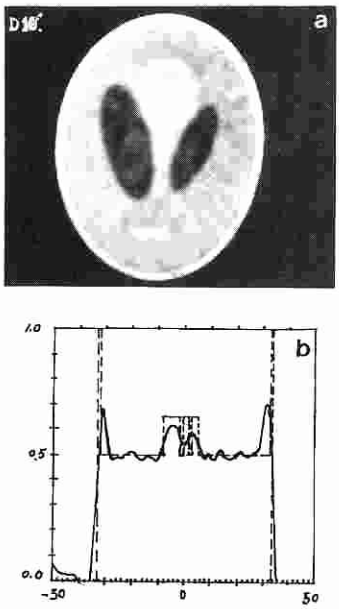

Fig.15 (a) The reconstructed 128x128 image with 360° rotated plane-wave insonification (Nearest-neighbor) (b) Numerical comparison on the line y=-0.605 (See Fig.5)

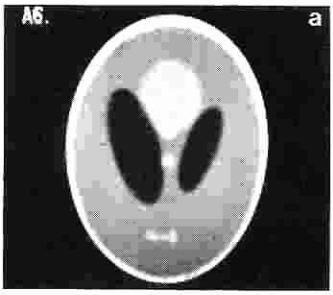

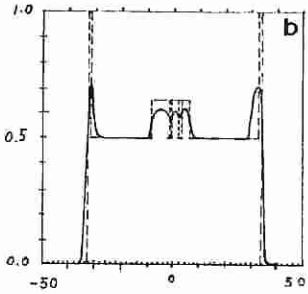

Fig.16 (a) The 128x128 image reconstructed from the windowed 128x128 Fourier-domain grids (delta=2√2kΩ/128) (b) numerical comparison on the line y=-0.605 (See Fig.5)

Fig.13, and this indicates that the information obtained from the 256x256 diffracted data for the SADCT are sufficient and the errors caused by the reconstruction algorithm itself is very small, provided that the weak scattering assumption is satisfied and the data obtained by the measuring system are sufficiently accurate.

For the conventional DUCT, the conclusion that the nearest-neighbor interpolation algorithm is better than the bilinear interpolation algorithm is not true. Fig.14 and 15 are the reconstructed images obtained by the conventional DUCT, and Fig.16 is the image reconstructed by the direct

Table 2. The distances of the images reconstructed by the bilinear and the nearest-neighbor interpolation reconstruction algorithms for the 360° rotated plane-wave insonified DUCT

Fig.	Interpolation	d1	r1	e1	d2	r2	e2	max	min
14	Bilinear	0.2910	0.1209	0.4100	0.2910	0.1209	0.4098	0.9436	-3.127×10^{-2}
15	Nearest-neighbor	0.3105	0.1895	0.4298	0.3105	0.1897	0.4292	0.9926	-8.233×10^{-2}
16	Direct calculation	0.2725	9.151×10^{-2}	0.3789	0.2725	9.186×10^{-2}	0.3788	0.9861	-1.880×10^{-4}

calculation of the Fourier transform of the object function on the rectangular grids. The conditions of the reconstruction of the image in Fig.16 are the same as those in Fig.13 except for delta=$2\sqrt{2}k_0/128$ (the radius of the blackman window is kept the same). The distances of the reconstructed images of Fig.14 to 16 are shown in Table 2.

From Fig.14, Fig.15 and Table 2, we can see that the image reconstructed by the bilinear interpolation algorithm is superior than that reconstructed by the nearest-neighbor interpolation. By the way, we can see that the image in Fig.16 is superior than that in Fig.13. This is because the image in Fig.16 contains more grid points in Fourier space than the image in Fig.13.

Figs.17, 18 and 19 are the moduli of the 128x128 spectra of the object obtained by the bilinear interpolation, the nearest-neighbor interpolation (N=128) and the direct calculation, respectively. They are corresponding to Figs.7, 10 and 13, respectively. In order to show the details of the spectra, we assigned those values which were greater than 2 to 2 in the spectra (the maximan value in these spectra was about 20 and occured at the center of these spectra). From these spectra, we can see that in the case of SADCT, the spectrum obtained by the nearest-neighbor interpolation is more accurate than that obtained by the bilinear interpolation, especially in the overlaped regions of the Fourier coverage areas A and B. This is why for SADCT, the nearest-neighbor interpolaiton gives better reconstructions.

Fig.17 The 128x128 spectrum image obtained by the bilinear interpolation (N=128). (before windowing)

Fig.18 The 128x128 spectrum image obtained by the nearest-neighbor interpolation (N=128). (before windowing)

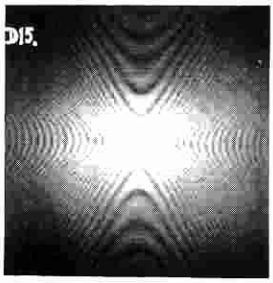

Fig.19 (a) The 128x128 spectrum image obtained by direct calculations (Before windowing)

Shift of Coordinate before and after Interpolations

Because we take the coordinate system shown in Fig.1, the center of the object is located at point (0,d/2). Therefore, the coordinate of the object must be shifted in Fourier domain before the 2-D IFFT is performed (the shift of the coordinate of the object in the Fourier domain is fulfiled simply by multiplying the spectrum of the object with a phase factor).

In the computer simulation, we discovered that the order of the shift of the coordinate and the interpolations had a great influence on the reconstructed images. The shift of the coordinate before the interpolations was better than the shift of the coordinate after the interpolations. Figs.20 and 21 show the images reconstructed by the bilinear and the nearest-neighbor interpolation algorithms, respectively, with the shift of the coordinate after the interpolations. Table 3 gives the comparison of the distances of these images and the images shown in Figs.7 and 10.

From Fig.20 we can see that there are noticeable unsymmetrics in the reconstructed image as compared with Fig.7, and, from Fig.21 we can see that artifacts are increased in the reconstructed image as compared with Fig.10. In Table 3, we will see that the distances for Figs.20 and 21 are increased greatly. These results indicate that the qualities of the reconstructed images will be degraded if the shift of the coordinate is performed after the interpolations.

With and Without Special Considerations of the Points Near the Boundaries

In the computer simulation, we also discovered that for SADCT, the accuracy of the interpolations of the points near the boundaries in the Fourier-domain coverage areas A or B (see Fig.2) had a great influence on the reconstructed images. This can be illustrated by Fig.22.

From Fig.22, we can see that the distributions of the discrete points on which the Fourier transform of the object is known are highly uneven. Near the axes of the rectangular coordinate, the points distribute densely, while in the areas near the boundaries of the Fourier-domain coverage areas A or B, the points distribute sparsely. Therefore, the interpola-

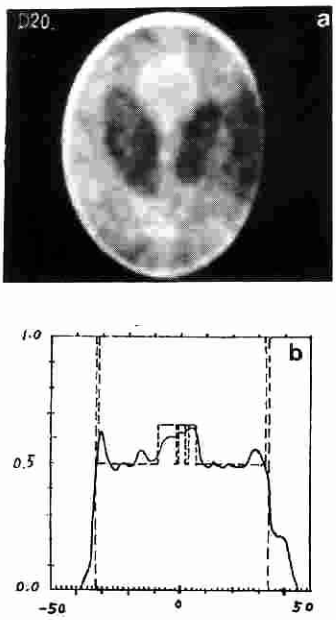

Fig.20 (a) The reconstructed 128x128 image with N=128 for the SADCT. The coordinate was shifted after the bilinear interpolation. (b) Numerical comparison on the line y=-0.605 (See Fig.5)

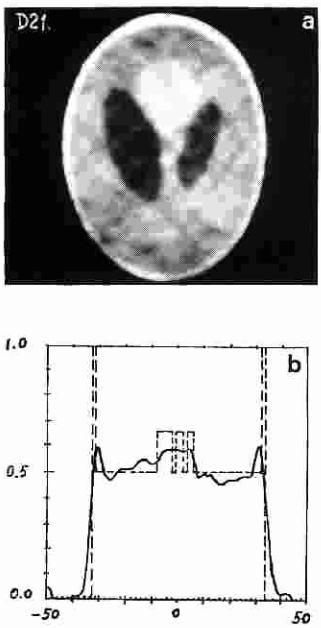

Fig.21 (a) The reconstructed 128x128 image with N=128 for the SADCT. The coordinate was shifted after the nearest-neighbor interpolation. (b) Numerical comparison on the line y=-0.605 (See Fig.5)

tions of the points near the boundaries will be less accurate than those near the axes.

The special considerations of the points near the boundaries are as follows. Rather than interpolate the points near the boundaries by averaging two interpolation results obtained from the areas A and B respectively as described in previous section, we interpolate the points near the boundary of the area A by the data in the area B, and vice versa. This will produce better results because a point near the boundary of one area will be the point near the axis in another (because the high values of the spectrum are concentrated in the low-

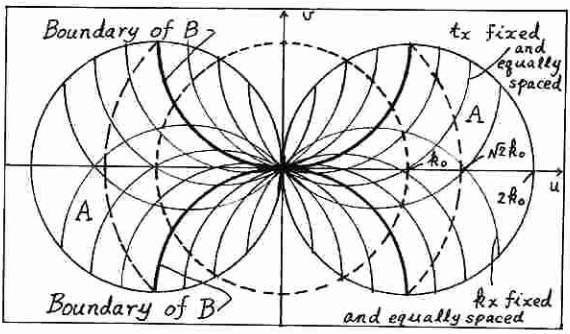

Fig.22 The distributions of the known values on the curvilinear coordinate for the SADCT

Table 3. The distances of the images reconstructed by the FDIRAs for the SADCT (coordinate shift after the interpolations)

Fig.	N	Specifications	d1	r1	e1	d2	r2	e2	max	min
20	128	Coordinate shifted after bilinear interpolation	0.4990	0.3591	0.7446	0.4990	0.3592	0.7445	0.8414	-0.2446
7	128	Coordinate shifted before bilinear interpolation	0.4659	0.3179	0.6089	0.4659	0.3179	0.6087	0.8364	-0.1203
21	128	Coordinate shifted after nearest-neighbor interpolation	0.3596	0.2017	0.5084	0.3596	0.2017	0.5082	0.9795	-9.540×10^{-2}
10	128	Coordinate shifted before nearest-neighbor interpolation	0.3367	0.1634	0.4617	0.3367	0.1634	0.4616	0.9202	-4.976×10^{-2}

frequency region, we just consider mainly those points in the region of lower frequency). In practical implementation of the interpolations of the points near the boundaries, we must decide which points are those near the boundaries. We solved this problem by experiments. As a result, we interpolated the points near the boundary of one area by the data in another when the conditions $|t_x| \geqslant k_0/32$ or $|k_x| \geqslant k_0/32$ were satisfied. Figs.23 and 24 are the reconstructed images obtained by the Fourier-domain bilinear and nearest-neighbor interpolations respectively, and with no specical considerations of the points near the boundaries (i.e., the interpolations of a point near the boundary of one area is performed by the data in the same area, then, if the point is in the intersections of two areas, the results of the interpolations obtained from these two areas are averaged).

Table 4. The distances of the images reconstructed by the FDIRAs for the SADCT (no considerations of the vicinity points of the boundaries)

Fig.	N	Specifications	d1	r1	e1	d2	r2	e2	max	min
7	128	Bilinear interpolation with the considerations of the vicinities of the boundaries	0.4659	0.3179	0.6089	0.4659	0.3179	0.6087	0.8364	-0.1203
23	128	Bilinear interpolation with no considerations of the vicinities of the boundaries	0.4935	0.3287	0.6660	0.4935	0.3288	0.6659	0.7883	-0.1204
10	128	Nearest-neighbor interpolation with the considerationsof the vicinities of the boundries	0.3367	0.1634	0.4617	0.3367	0.1634	0.4616	0.9209	-4.976×10^{-2}
24	128	Nearest-neighbor interpolation with no considerations of the vicinities of the boundaries	0.3740	0.2151	0.5416	0.3740	0.2152	0.5415	0.9120	-0.1095

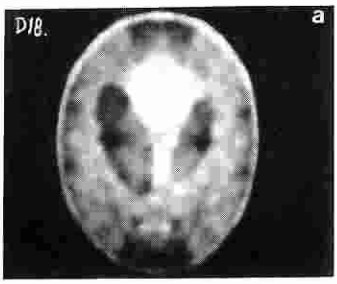

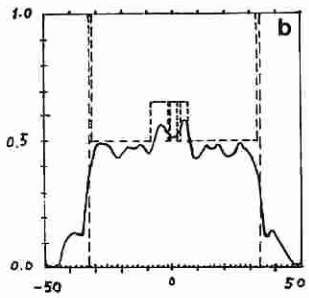

Fig.23 (a) The reconstructed 128x128 image with N=128 for the SADCT (bilinear). No special considerations of those points in the vicinities of the boundaries (b) Numerical comparison on the line y=-0.605 (See Fig.5)

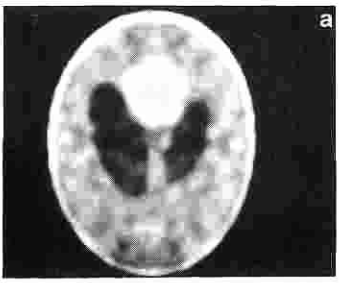

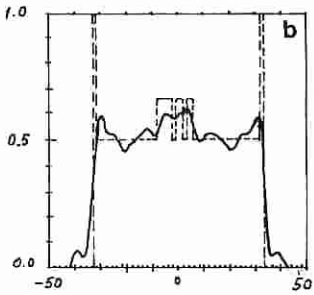

Fig.24 (a) The reconstructed 128x128 image with N=128 for the SADCT (nearest-neighbor). No special considerations of those points in the vicinities of the boundaries (b) Numerical comparison on the line y=-0.605 (See Fig.5)

From Figs.23 and 24, we can see that the reconstructed images degraded greatly as compared with figs.7 and 10 respectively (Fig.7 and 10 are the images reconstructed with the special considerations of the points near the boundaries of the areas A and B using the method described above). In Table 4, we can see that the values of the distances for Figs.23 and 24 are increased remarkably.

For the results obtained by the shift of coordinate after the interpolations and, at the same time, with no special considerations of the points near the boundaries, the readers may refer to reference [18].

SUMMARY

In this paper, we have made a detailed study of FDIRAs for SADCT, and, the results of the study has been compared with those obtained by IFRA developed by Dr. D.Nahamoo et al..

The major conclusion of our computer simulation study is in the following :

(1) The number of the complex multiplications has been greatly reduced from the order $O(N^3+N^2\log_2 N)$ for IFRA derived by Dr. D.Nahamoo at el. to $O(N^2\log_2 N)$ for FDIRAs for an NxN image reconstructed from NxN diffracted data. (For N=128, VAX-11/730 CPU processing time were 2.61 min (bilinear) and 2.57 min (nearest-neighbor) for FDIRAs and 19.28 min for IFRA).

(2) FDIRAs gives better reconstructions than IFRA.

(3) For FDIRAs of SADCT, the nearest-neighbor interpolation reconstruction algorithm will give better results than the bilinear interpolation, but, it is not the case in the conventional DUCT.

(4) For FDIRAs of SADCT, the shift of the coordinate of the object must be performed before the Fourier-domain interpolations, otherwise, the quality of the reconstructed images will be degraded.

(5) The accuracy of the interpolations of the points near the boundaries of the Fourier-domain coverage areas has a great influence on the reconstructions. Therefore, to ensure a good image reconstruction, the interpolations of these points must be specially considered.

(6) In this paper, all the reconstructed images have been evaluated by the distance criteria, and these criteria are well coincidence with the quality of the reconstructed images.

(7) The relationships between the curvilinear coordinate and the rectangular coordinate for SADCT are not so straightforward as compared with the conventional DUCT. It depends on which quarter of the Cartesian coordinate and which area of the Fourier-domain coverages a point (u,v) on the rectangular coordinate belongs to.

(8) For SADCT with N=256, the Fourier transform of the diffracted data will provide sufficient information of the Fourier transform of the object, and the nearest-neighbor interpolation reconstruction algorithm itself will cause little distortion and will produce a reconstruction close to the limit reconstruction (see Fig.13).

(9) The disadvantage of SADCT is that the distribution of the points on which the Fourier transform of the object are known are highly uneven as compared with the conventional DUCT [11], and, thus, more diffracted data are required for SADCT to obtain the same reconstruction quality as the conventional DUCT.

ACKNOWLEDGEMENT

The author is gratitude to Prof. Yu Wei, the author's doctoral supervisor, in Department of Biomedical Engineering, Nanjing Institue of Technology (who is now the president of the Institute) for her many suggestions in this work, such as, to adopt the distance critera for the quantitative evaluations of the reconstructed images. The author is also gratitude to Miss Li Lin, a graduated student in the Pharmacy University of China, for her help in drawing many figures in this paper.

REFERENCES

1. L. Axel, P.H. Arger, and R.A. Zimmerman, "Applications of Computerized Tomography to Diagnostic Radiology", Proceedings of IEEE, Vol. 71, No. 3, March 1983, pp. 293-297.
2. D.P. Boyd and M.J. Lipton, "Cardiac Computerized Tomography", Proceedings of IEEE, Vol. 71, No. 3, March 1983, pp. 308-319.
3. R.A. Robb, E.A. Hoffman, L.J. Sinak, L.D. Harris, and E.L. Ritman, "High-Speed Three-Dimensional X-Ray Computed Tomography", Proceedings of IEEE, Vol. 71, No. 3, March 1983, pp. 308-319.
4. H.T. Bates, K.L. Garden, and T.M. Peters, "Overview of Computerized Tomography with Emphasis on Future Developments", Proceedings of IEEE, Vol. 71, No. 3, March 1983, pp. 356-372.
5. J.K. Udupa, "Display of 3D Information in Discrete 3D Scenes Produced by Computerized Tomography", Proceedings of IEEE, Vol. 71, No. 3, March 1983, pp. 420-431.
6. P. Bloch and J.K. Udupa, "Application of Computerized Tomography to Radiation Therapy and Surgical Planning", Proceedings of IEEE, Vol. 71, No. 3, March 1983, pp. 351-355.
7. G.T. Herman, "Image Reconstruction from Projections", Academic Press, 1980.
8. J.F. Greenleaf, "Computerized Tomography with Ultrasound", Proceedings of IEEE, Vol. 71, No. 3, March 1983, pp. 330-337.
9. R.K. Mueller, M. Kaveh, and G. Wade, "Reconstructive Tomography and Applications to Ultrasonics", Proceedings of IEEE, Vol. 67, No. 4, 1979, pp. 567-587.
10. R.K. Mueller, M. Kaveh, and R.D. Iverson, "A New Approach to Acoustic Tomography Using Diffraction Techniques", Acoustical Imaging, A.F. Metherell, ed., Vol. 8, 1980, pp. 615-629.
11. S.X. Pan, and A.C. Kak, "A Computational Study of Reconstruction Algorithms for Diffraction Tomography: Interpolation Versus Filtered-Backpropagation", IEEE Transactions on Acoustical Speech Signal Processing, Vol. ASSP-31, 1983, pp. 1262-1276.
12. Cong-Qing Lan, Gail T. Flesher, and Glen Wade, "Plane-Scanning Reflection-Diffraction Tomography", IEEE Transactions on Sonics and Ultrasonics, Vol. SU-32, No. 4, July 1985, pp. 562-565.
13. A.J. Devaney, "A Filtered-Backpropagation Algorithm for Diffraction Tomography", Ultrasonic Imaging, Vol. 4, 1982, pp. 336-350.
14. A.J. Devaney, "A Computer Simulation Study of Diffraction Tomography", IEEE Transactions on Biomedical Engineering, Vol. BME-30, No. 7, July 1983, pp. 377-386.
15. D. Nahamoo, S.X. Pan, and A.C. Kak, "Synthetic Aperture Diffraction Tomography and Its Interpolation-Free Computer Implementation", IEEE Transactions on Sonics and Ultrasonics, Vol. SU-31, No. 4, July 1984, pp. 218-229.
16. D. Nahamoo and A.C. Kak, "Ultrasonic Diffraction Imaging", Tech. Rep. TR-EE-82-20, School of Electrical Engineering, Purdue University.
17. D.J. Vezzetti and S.Ø. Aks, "Reconstruction from Scattering Data: Analysis and Improvements of the Inverse Born Approximation", Ultrasonic Imaging, Vol. 1, 1980, pp. 335-345.
18. Jian-Yu Lu, "A Study of the Fourier-Domain Reconstruction Algorithms for Synthetic Aperture Diffraction Tomography", Proceedings of China-Japan Joint Conference on Ultrasonics, May 11-14, 1987, Nanjing, China, Edited by the Organizing Committee.
19. J.W. Goodman, "Introduction to Fourier Optics", McGraw-Hill, New York 1968, Chapter 3.
20. P.M. Morse and K.V. Ingard, "Theoretical Acoustics", McGraw-Hill, 1968, Chapter 8.

21. P.M. Morse and H. Feshbach, "Methods of Theoretical Physics", McGraw-Hill, 1953, p. 823.
22. L.A. Shepp and B.F. Logan, "The Fourier Reconstruction of a Head Phantom", IEEE Transactions on Nuclear Science, Vol. NS-21, 1974, pp. 21-43.